

## Accepted Manuscript

Effects of collagen microstructure and material properties on the deformation of the neural tissues of the lamina cribrosa

A.P. Voorhees, N.-J. Jan, I.A. Sigal

PII: S1742-7061(17)30334-3

DOI: <http://dx.doi.org/10.1016/j.actbio.2017.05.042>

Reference: ACTBIO 4901

To appear in: *Acta Biomaterialia*

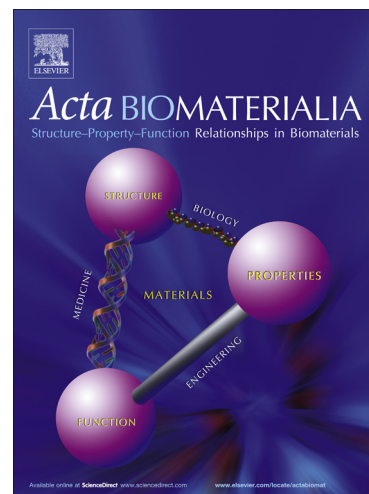
Received Date: 4 March 2017

Revised Date: 3 May 2017

Accepted Date: 17 May 2017

Please cite this article as: Voorhees, A.P., Jan, N.-J., Sigal, I.A., Effects of collagen microstructure and material properties on the deformation of the neural tissues of the lamina cribrosa, *Acta Biomaterialia* (2017), doi: <http://dx.doi.org/10.1016/j.actbio.2017.05.042>

This is a PDF file of an unedited manuscript that has been accepted for publication. As a service to our customers we are providing this early version of the manuscript. The manuscript will undergo copyediting, typesetting, and review of the resulting proof before it is published in its final form. Please note that during the production process errors may be discovered which could affect the content, and all legal disclaimers that apply to the journal pertain.



# Effects of collagen microstructure and material properties on the deformation of the neural tissues of the lamina cribrosa

A.P. Voorhees<sup>1</sup>, N.-J. Jan<sup>1,2</sup>, and I.A. Sigal<sup>1,2,3\*</sup>

<sup>1</sup> Department of Ophthalmology, UPMC Eye Center, Eye and Ear Institute,  
Ophthalmology and Visual Science Research Center

University of Pittsburgh School of Medicine, Pittsburgh, PA, USA

<sup>2</sup> Department of Bioengineering, Swanson School of Engineering,  
University of Pittsburgh, Pittsburgh, PA, USA

<sup>3</sup> McGowan Institute for Regenerative Science  
University of Pittsburgh School of Medicine, Pittsburgh, PA, USA

**Short Title:** Lamina Cribrosa Neural Tissue Deformation

**\* Correspondence:**

Ian A. Sigal, Ph.D.

Ocular Biomechanics Laboratory,

Department of Ophthalmology, University of Pittsburgh School of Medicine, Pittsburgh, PA.

203 Lothrop Street, Rm 930, Pittsburgh PA, 15213.

ian@OcularBiomechanics.com (412) 864-2220

www.ocularbiomechanics.org

**Key Words:** lamina cribrosa, optic nerve head, biomechanics, glaucoma, microstructure, finite element modeling, intraocular pressure.

**Proprietary Interest:** None

**Grant Information:** Supported in part by National Institutes of Health grants R01-EY023966, R01-EY025011, P30-EY008098 and T32-EY017271 (Bethesda, MD) and the Eye and Ear Foundation (Pittsburgh, PA).

**Number of Words:** 5753

**For submission to Acta Biomaterialia**

**ABSTRACT** [ 223 words]

It is widely considered that intraocular pressure (IOP)-induced deformation within the neural tissue pores of the lamina cribrosa (LC) contributes to neurodegeneration and glaucoma. Our goal was to study how the LC microstructure and mechanical properties determine the mechanical insult to the neural tissues within the pores of the LC. Polarized light microscopy was used to measure the collagen density and orientation in histology sections of three sheep optic nerve heads (ONH) at both mesoscale (4.4  $\mu\text{m}$ ) and microscale (0.73  $\mu\text{m}$ ) resolutions. Mesoscale fiber-aware FE models were first used to calculate ONH deformations at an IOP of 30 mmHg. The results were then used as boundary conditions for microscale models of LC regions. Models predicted large insult to the LC neural tissues, with 95<sup>th</sup> percentile 1<sup>st</sup> principal strains ranging from 7-12%. Pores near the scleral boundary suffered significantly higher stretch compared to pores in more central regions ( $10.0 \pm 1.4\%$  vs.  $7.2 \pm 0.4\%$ ;  $p=0.014$ ; mean  $\pm$  SD). Variations in material properties altered the minimum, median, and maximum levels of neural tissue insult but largely did not alter the patterns of pore-to-pore variation, suggesting these patterns are determined by the underlying structure and geometry of the LC beams and pores. To the best of our knowledge, this is the first computational model that reproduces the highly heterogeneous neural tissue strain fields observed experimentally.

## 1. Introduction

Glaucoma is a progressive neurodegenerative disease resulting in the death of retinal ganglion cells (RGC) and irreversible vision loss. While the exact causes of glaucomatous damage are not entirely clear [1-4], there is a strong association between glaucoma progression and elevated intraocular pressure (IOP) [5]. In fact the only accepted treatments for glaucoma focus on lowering IOP [6]. Experimental evidence has shown that glaucomatous damage initiates in the lamina cribrosa (LC) [7], a complex structure in the posterior pole consisting of collagenous beams and neural tissue pores containing both RGC axons and glial cells (Fig. 1). Thus, most theories regarding the initiation and progression of glaucoma center around excessive IOP-induced mechanical deformation or stress within the lamina cribrosa (LC) [3, 4].

Much work has gone into modeling the complex structures of the optic nerve head (ONH), the region of the eye including the LC where the RGC axons converge to form the optic nerve, in an attempt to understand how the LC and other tissues of the ONH deform under elevated IOP [8-14]. Over the last ten years, efforts have primarily focused on developing models that include the effects of collagen fiber alignment and material non-linearity [13-15], both improvements upon earlier isotropic linear models [9, 10, 16]. Despite these advances, there have been no eye-specific LC models that explicitly consider the neural tissues independent of the connective tissue. This is a major limitation because it is the mechanical insult to the neural tissues that is hypothesized to lead to neurodegeneration, and the models cannot predict that insult. Moreover, previous models have lumped the neural tissues and connective tissue microstructure together. Not surprisingly, the models have been unable to reproduce the strain fields observed experimentally. Recent models predict tensile strains within the LC to be less than 5% under elevated levels of IOP [10, 13, 14, 16, 17], whereas experimental studies by us [18, 19] and others [20] have measured IOP-induced strains exceeding 10 and even 20% in some regions. Further, these experiments revealed highly heterogeneous deformation fields, with levels of stretch varying greatly from one LC pore to another.

Our goal was to study how the LC neural tissues deform under elevated IOP and how the material properties of the LC and peripapillary sclera influence the level of mechanical insult. Since these are the tissues actually injured in glaucoma, determining how they deform and the role of the collagenous LC microstructure in mitigating or antagonizing this deformation is essential for understanding glaucoma susceptibility and progression. To accomplish this goal, we made highly detailed, multiscale, specimen-specific models of the LC that included both collagenous laminar beams and neural tissue.

## 2. Methods

We used a two-level modeling approach. First we modeled the ONH at a mesoscale level (mean element edge length of 112  $\mu\text{m}$ ), using serial histological sections of the ONH and peripapillary sclera, similar to previous approaches [13, 14]. These models were then used as boundary conditions for high resolution, microscale models of LC regions (mean element edge length of 7-10  $\mu\text{m}$ ) which included distinct material properties for LC neural tissues and beams. We conducted a sensitivity analysis in which we varied the material properties of both the neural tissues and connective tissues both to test the robustness of our conclusions to our choice of material properties and to understand the influence of the material properties on the neural tissue strains.

### 2.1 Histology

Three eyes from two sheep were obtained from a local abattoir. All histological methodology has been described elsewhere [21, 22]. Briefly, eyes were pressure fixed via cannulation through the anterior chamber at 5 mmHg with a gravity column and bath of 10% formalin overnight. Posterior poles centered on the ONH were removed with a 11.5 mm trephine and cryosectioned coronally into 30  $\mu\text{m}$  thick sections. Sections were collected serially through the depth of the tissue. It should be noted that the tissue was neither stained nor dehydrated. We have demonstrated our tissue processing protocol including formalin fixation and sectioning generally preserves both the shape and size of ocular tissues [21].

### 2.2 Imaging

An overview of our multiscale imaging approach can be found in Fig. 2. All imaging methods have been previously described [21, 22]. Briefly, polarized filters were used in conjunction with a bright-field microscope. Images were collected with the filters in several orientations, and from these images we calculated the orientation of the collagen fibers at each pixel and the energy (an optical measure related to collagen density) [21].

Mesoscale histology images were taken with an Olympus SZX16 microscope (Olympus, Tokyo, Japan) and an Olympus DP80 camera with a 0.8x objective and 1x magnification setting (4.4  $\mu\text{m}$  per pixel). Microscale images were taken with an Olympus BX60 microscope with a SPOT camera (SPOT imaging Solutions, Sterling Heights, MI) with a 10x objective (0.73  $\mu\text{m}$  per pixel). Images were stitched together to produce larger mosaic images [23, 24]. Serial mesoscale histology images were manually registered to one to ensure section alignment. Microscale images were registered to mesoscale images by fitting an affine transformation to

manual markings of corresponding points. We have established the robustness of the methods to magnification [21].

### *2.3 Mesoscale model*

Our modeling approach is outlined in Fig. 3. For each eye, several sections through the ONH were chosen for use in the construction of the mesoscale models. Sections with large folds or tears were excluded from the model. The number of sections used for each eye model ranged from 6-11. Average pixel energy and average pixel orientation (circular mean) through the depth of the ONH were calculated using Matlab to create a 2D representation of the 3D structure. Any small tears or missing regions were manually excluded from the through-thickness averages. In one sample, two narrow cuts were made during sectioning and pixels in this region of the through-thickness averaged data were assigned energy values based on a linear interpolation and orientation values based on a nearest neighbor interpolation. A circular region of the thickness-averaged ONH was selected for modeling.

For our mesoscale models we followed an approach similar to the one by Zhang et al. [13], however the ONH was modeled as a circular disk, with a thickness equal to 5% of the diameter rather than a square. To create the finite element mesh, a regularly spaced triangular mesh of a circle with dimensions equal to the size of the circular ONH region was created so that the average number of pixels per element was approximately 200. The triangular mesh was then replicated five times and shifted along the out of plane direction to create a six-layer point set. A constrained Delaunay tetrahedralization was conducted to create a quadratic tetrahedral mesh. The mean energy and mean element fiber orientation for each element was calculated from the thickness averaged image. The mean element energy was used to weight the stiffness of each element and the mean element fiber orientation was used to define the direction of maximal stiffness as will be defined in more detail in the material properties section of the methods.

To simulate the effects of IOP, a uniform outward boundary pressure was applied to the edges of the disk to mimic the effects of hoop stress as done by Zhang et al. [13]. However, when considering the dimensions of the sheep eye, we found that the hoop stress for sheep eyes was 10x IOP. Thus to model an IOP of 30 mmHg, a boundary pressure of 300 mmHg was applied (39.9 kPa). The model was constrained in z along one face to create a symmetry boundary condition and the model was constrained at the edges to prevent rotation about the out-of-plane direction.

### *2.4 Microscale model*

Seven regions ( $\sim 0.3\text{-}0.9\text{ mm}^2$ ) with clearly defined collagen beams and no evidence of histological artifacts, such as broken or missing tissue or section folds were selected (Fig. 4). Four of these regions were taken from central regions of the LC and three regions were selected on the periphery of the LC. The three peripheral regions included parts of the sclera. For simplicity, models will be referenced by the letters A-G, as defined in Fig. 4. Note that A-G corresponds to increasing levels of connective tissue volume fraction (CTVF), so that model A has the lowest ratio of collagen to neural tissue and model G has the largest. Energy information from polarized light microscopy was used as the basis for 2D image segmentation. The contrast of each image was enhanced first by local contrast enhancement, and second by a histogram adjustment. An intensity based threshold was used to segment the collagen beams and the background (neural tissue). Segmented masks were edited manually to correct for local defects including those due to the presence of pigment. Small beams that appeared unconnected on one end were removed from the mask, as we could not be sure that these were in the plane of the sample. Masks were checked by three different researchers prior to being used for models.

The skeleton of the segmented image was calculated [23, 25], and errors in the skeletonized images due to centerline splitting near the edges of the segmented image were manually corrected. In-house code was used to generate a 3D reconstruction of the LC beams from the segmented image and the skeleton image (Fig. 2). Briefly, for each pixel of the skeleton the distance to the nearest segmented edge was calculated and a sphere in 3-dimensional space with this radius was added to a volumetric mask. The result of this procedure was a network of collagenous beams with circular cross-sections. The thickness of the volumetric image was chosen to be 5% thicker than the diameter of the largest collagen beam. Rather than use a simple 2D cross-section we chose this 3D approach as it better approximates the actual LC, improving predictions of strain near the beams (Supplementary Material). For computational simplicity, only half of the volume was actually modeled and symmetry boundary conditions were used.

A tetrahedral mesh of the binary volumetric images was created and mean fiber orientation was assigned to each element of the mesh by nearest neighbor interpolation from the polarized light microscopy fiber orientation data. Material properties were chosen for the collagen beams and neural tissues as described later in the Material properties section of the Methods. Displacement driven boundary conditions were obtained by linearly interpolating the displacements predicted from the mesoscale models to the locations of nodes on the sides of the mesh.

## 2.5 Material properties

The material properties of the neural tissue and of the collagenous beams were modeled using a fiber-based constitutive equation of the form

$$W = W_{Fiber} + W_{Ground}. \quad (\text{Eq. 1})$$

$W$  is the total strain energy density,  $W_{Fiber}$  is the strain energy density of the anisotropic fibers (collagen fibers for the LC beams or cytoskeletal filaments for the neural tissue), and  $W_{Ground}$  is the isotropic strain energy density of the ground substance. The strain energy density of a fiber was modeled using an exponential power law with the form

$$w_{Fiber} = \frac{\xi}{2\alpha} \left( \exp \left[ \alpha (\lambda_n^2 - 1)^2 \right] - 1 \right). \quad (\text{Eq. 2})$$

$\xi$  is a linear material constant defining the linear stiffness of the fibers,  $\alpha$  is a non-linear material constant that governs how the stiffness of the fibers changes with the stretch of the fiber, and  $\lambda_n$  is the fiber stretch. The strain energy density for all fibers was then calculated as the sum of the strain energy density for all fibers using the equation

$$W_{Fiber} = \int_{-\pi}^{\pi} H(\lambda_n - 1) \cdot p(\theta_n) \cdot w_{Fiber} \cdot d\theta_n. \quad (\text{Eq. 3})$$

$H$  is a Heaviside function used to ensure that fibers are unstressed in compression,  $p$  is the probability density function used to describe the relative number of fibers with a given orientation, and  $\theta_n$  is the orientation of an individual fiber. The strain energy density equation for the ground material was modeled as a Mooney-Rivlin solid which has the form.

$$W_{Ground} = C_1(I_1 - 3) + C_2(I_2 - 3) + \frac{1}{2}K(\ln J)^2. \quad (\text{Eq. 4})$$

$C_1$  and  $C_2$  are material constants defining the stiffness of the material and  $I_1$  and  $I_2$  are the first and second invariants of the right Cauchy-Green deformation tensor (non-directional measures of material deformation),  $K$  is the bulk modulus which defines the compressibility of the material and  $J$  is the Jacobian of the deformation gradient which is a measure of the volume change of the material. For the collagenous material, the parameter  $C_2$  was set to zero which is analogous to a neo-Hookean formulation. Collagenous material was modeled using a nearly incompressible constitutive formulation, while neural tissue was modeled as a compressible material. The strain energy density for the material properties for the collagenous tissue were fit to experimental data obtained for human sclera via inflation testing [15]. For collagenous material the fibers were modeled using a 3D  $\pi$ -periodic von Mises distribution with concentration parameter  $\kappa$ . High values of  $\kappa$  represent highly aligned fibers, and 0 represents a perfectly uniform distribution of fibers. For the mesoscale models  $\kappa$  was chosen to be 0.6 to match the values reported in the literature for sclera [15]. For the microscale models  $\kappa$  was



chosen to be 2, representing a narrower distribution of fibers at the microscale level. The mean collagen fiber orientation was calculated based on the polarized light microscopy data, as described above. Neural tissue fibers were modeled as a perfectly aligned distribution of fibers oriented out of the plane of the model (following the path of the optic nerve) with material properties based on guinea pig white matter [26]. The parameters used for our baseline studies appear in Table 1.

For the mesoscale models material properties were assigned by weighting the strain energy density function of the collagen material by the energy data from the thickness-averaged histology measurements. The weighting was chosen so that any element with an average energy value equal to the average energy value of the entire sclera would have the material properties defined in Table 1 for collagenous material. Thus, the weighting of the material properties has the following form

$$W_{Elem} = \frac{E_{Elem}}{\bar{E}_{Elem}} (W_{Fiber} + W_{Ground}). \quad (\text{Eq. 4})$$

$E_{Elem}$  is the element averaged energy and  $\bar{E}_{Elem}$  is the energy averaged over the entire sclera of the section. Average element energy was rounded to two decimal places, so that any elements could be defined by 1 of a set of 100 different material properties.

### 2.6 Material properties sensitivity analysis

Since the material properties of the collagenous beams and neural tissue of the sheep LC have not been experimentally determined, we varied the material properties used in our models to understand what effects they might have on our findings. This also provides a means for studying the effects of changes in material properties of the sclera and LC that are known to change with age and disease [27-30]. To understand the effect of neural tissue stiffness, we tested the effects of a 10x increase in neural tissue stiffness for model G. Since, neural tissue stiffness is not included in the formulation of the mesoscale models, this test did not require the mesoscale model to be rerun. We also varied the material properties of the collagen beams. We tested four different material properties variations: 1) Stiff (representing a doubling of collagen stiffness), 2) Compliant (representing a halving of collagen stiffness), 3) Non-Linear (representing a doubling of fiber non-linearity while maintaining the same level of stress under 2% equibiaxial stretch, and 4) Linear (representing no fiber non-linearity while maintaining the same level of stress under 2% equibiaxial stretch). The parameter values used for these cases appear in Table 2. For these variations models were re-run at both the mesoscale and microscale level. Finally, we tested the effect of collagen fiber dispersion on the results of our models, since we did not directly measure this dispersion from histology. Three additional cases

were tested: 1) Isotropic fiber distribution ( $\kappa=0$ ), 2) Wide fiber distribution ( $\kappa=0.5$ ), and 3) Perfectly aligned fibers ( $\kappa=\infty$ ). For this case, we did not rerun the mesoscale models, since the choice of  $\kappa=0.6$  was based on measurements for sclera from the literature and fiber orientation would be expected to vary more over the larger elements of the mesoscale models.

### *2.7 Mechanical Analysis*

To eliminate edge effects, elements located within 10% of the total region length or width from an edge were excluded from the analysis. Additionally, only elements on the symmetry plane were considered in the analysis of strain distribution. This was done to ensure that our conclusions were not overly influenced by our assumptions about tissue structure in the out of plane direction. 1<sup>st</sup> principal and 2<sup>nd</sup> principal strains and stresses were calculated from in plane strain and stress components only. Thus, the first principal strains represent the stretch of the tissue and the second principal strains represent tissue compression. The difference between the 1<sup>st</sup> and 2<sup>nd</sup> principal strains is a measure of the maximum shear strain. All stresses and strains are reported with respect to the deformed geometry, with stresses being reported as Cauchy stress in kPa and all strains being reported as Green strain reported as a percent, i.e. Green strain multiplied by 100. All median and percentile calculations were conducted using volume-weighted methods.

### *2.8 Statistical methods*

Median and maximum (95<sup>th</sup> percentile) 1<sup>st</sup> principal neural tissue strain and median and minimum (5<sup>th</sup> percentile) 2<sup>nd</sup> principal neural tissue strain was compared between the central regions ( $n=4$ ) and peripheral regions ( $n=3$ ). A student's t test was used to test for statistical significance. Data for these comparisons is presented as mean  $\pm$  standard deviation.

### *2.9 Software*

FEBio v2.3.0 [31] was used for all finite element analysis. Paintshop Pro X2 (Corel, Ottawa, ON, Canada) was used for manual 2D segmentation of microscale models. Fiji [23-25] was used for 2D image skeletonization and analysis of polarized light microscopy images including image stitching. Custom code and the GIBBON [32] toolbox for Matlab (v2015b, Mathworks, Natick, MA) were used to create segmented volumes, register microscale models to mesoscale models, write FEBio input files and analyze data, including statistical analysis. Avizo Wind v8.0.1 (FEI, Hillsboro, OR) was used to register histological section images and create microscale meshes.

### 3. Results

#### 3.1 Microscale strains and stress for baseline conditions

The predicted strains for each of the microscale regions are shown in Fig. 5. Wide variation in the levels of 1<sup>st</sup> principal strain is seen from one pore to another. Within single pores some areas experienced very large 1<sup>st</sup> principal strains, exceeding 15%. The distributions of the 1<sup>st</sup> and 2<sup>nd</sup> principal strains are presented in Fig. 6. Median 1<sup>st</sup> principal strains were significantly greater in the regions at the LC periphery as compared to the central regions ( $5.6 \pm 0.5\%$  vs.  $4.0 \pm 0.4\%$ ;  $p=0.004$ ). Maximum 1<sup>st</sup> principal strains were also greater in the regions at the LC periphery ( $10.0 \pm 1.4\%$  vs.  $7.2 \pm 0.4\%$ ;  $p=0.014$ ). In fact, the highest predicted stretch occurred in the pores nearest the sclera in the peripheral models (Fig. 5, F and G). For most pores, the 2<sup>nd</sup> principal stretch was positive indicating a state of biaxial stretch. However, a few pores, mainly those near the periphery underwent compression in the direction of the 2<sup>nd</sup> principal strain, indicating a state of uniaxial tension and high shear. Although there was no statistically significant difference in the median 2<sup>nd</sup> principal neural tissue strain between the peripheral and central regions ( $1.0 \pm 0.3\%$  vs.  $1.5 \pm 0.3\%$ ;  $p=0.106$ ), there was a significant decrease in the minimum 2<sup>nd</sup> principal strain ( $-2.5 \pm 1.3\%$  vs.  $-0.2 \pm 0.7\%$ ;  $p=0.024$ ). Collagen underwent largely uniaxial tension in the “beam” parts, and biaxial tension in the beam intersections and in some thick beams.

The direction of the 1<sup>st</sup> principal strain in the beams was along the length of the beam and along the direction of the fibers, despite the fact that the beams were stiffer along the fiber direction than in the cross-fiber direction (Fig. 7). This finding was consistent across all the models. Since the direction of the 1<sup>st</sup> principal was along the beams, the direction of the 2<sup>nd</sup> principal was perpendicular to the beams and the native fiber orientation indicating beam thinning. In general, the direction of the 1<sup>st</sup> principal strain in the neural tissue pores was perpendicular to the longest surrounding beams. However, the direction of 1<sup>st</sup> principal strain was highly variable between one pore and its neighbor.

There was no clear pattern as to which types of beams experienced high stress concentrations and which did not (Fig. 8). Some, large beams had high stresses and some small beams had very small stress concentrations. Stresses did tend to be concentrated away from beam intersections and often on one side of the beam indicating bending. The stress concentrations in the beams appeared to be larger in the peripheral LC regions.

#### 3.2 Parametric Analysis

We found that increasing the stiffness of the neural tissue 10-fold lowered the 1<sup>st</sup> principal neural tissue strains and increased the 2<sup>nd</sup> principal strains, resulting in lower shear strains (Fig 9). A few small regions of pores were predicted to have greater 1<sup>st</sup> principal strains though. Increased neural tissue stiffness reduced the range of the strain distributions, decreasing the 75<sup>th</sup> and 95<sup>th</sup> percentile 1<sup>st</sup> principal strains and increasing the 5<sup>th</sup> and 25<sup>th</sup> percentile 2<sup>nd</sup> principal strains.

Four different variations in the properties of the collagenous materials were tested for region G (Fig.10). Increasing the stiffness reduced the 5<sup>th</sup>, 25<sup>th</sup>, median, 75<sup>th</sup> and 95<sup>th</sup> percentile 1<sup>st</sup> principal strains in the neural tissues while a more compliant collagenous material resulted in increased 1<sup>st</sup> principal strains. The linear model predicted slightly higher 75<sup>th</sup> and 95<sup>th</sup> percentile 1<sup>st</sup> principal strains and more negative 5<sup>th</sup> percentile and 25<sup>th</sup> percentile 2<sup>nd</sup> principal strains. Increasing the non-linearity of the fibers did not have a strong effect on the predicted neural tissue strains. Overall, the strains in the neural tissue were more sensitive to the stiffness of the collagen beams than to the stiffness of the neural tissue.

Finally, we examined the effect of fiber dispersion. The 1<sup>st</sup> principal strains predicted by models with isotropic fibers or a wide distribution of fibers were similar to the baseline case (Fig. 11). Models with perfectly aligned fibers predicted higher 75<sup>th</sup> and 95<sup>th</sup> percentile 1<sup>st</sup> principal strains and more negative 2<sup>nd</sup> principal strains in the neural tissues. Interestingly, in all three cases the 2<sup>nd</sup> principal strain in the beams was reduced as compared to the baseline case. As a whole, these results may seem non-intuitive for the perfectly aligned fibers case, however, they are primarily explained by the fact that the direction of the 1<sup>st</sup> principal strain was slightly altered in several of the beams. In fact, in many places the direction of the 1<sup>st</sup> principal strain in the beams was altered to be between 10 and 45 degrees from the fiber orientation. While the baseline case and the wide distribution cases have some fibers that are aligned up to 45 degrees from the mean orientation angle, there were no fibers aligned along this direction for the perfectly aligned case. Hence, the perfectly aligned fiber model allows for increased stretch in the collagen beams when the direction of loading slightly differs from the measured fiber direction.

#### 4. Discussion

Our goal was to study how the LC neural tissues deform under elevated IOP and how the material properties of the LC and peripapillary sclera influence the level of mechanical insult. Our numerical models predicted IOP-induced tensile and compressive strains within the neural tissues of the LC that were large and heterogeneous, varying greatly from one pore to another.

The stiffness and non-linearity of the connective tissue influenced the magnitudes of the strains in the neural tissues, however, the stiffness of the neural tissues and the anisotropy of the connective tissue had only minimal effects. Strains were significantly higher in pores near the periphery of the LC, adjacent to the lamina. Accurate characterization of the effects of IOP on the neural tissues of the LC is critical to understanding the pathogenesis and progression of glaucoma as the LC neural tissues are hypothesized to be damaged by IOP-induced mechanical insult. Our conclusions are largely in agreement with recent experimental testing which has predicted similar behavior [18-20].

Tensile (1<sup>st</sup> principal) strains in the neural tissues in the peripheral LC models, exceeded 10% (95<sup>th</sup> percentile). In the context of cell mechanobiology these levels of strain can be quite damaging. The astrocytes of the lamina cribrosa have mechanosensitive ion channels and are known to take on an activated remodeling phenotype when stretched [33, 34]. Exler and colleagues recently found that 12% biaxial stretch altered the phosphorylation of PEA-15 in astrocytes, which in turn promotes MMP activity and apoptosis [35]. This group has previously found that 12% stretch promotes the expression of Annexin A4, a protein associated with cell membrane repair, indicating potential cellular damage [36]. 20% strain of astrocytes is similar to the levels observed in mild traumatic brain injury which is known to reduce cell membrane integrity and trigger an inflammatory cascade including the expression of TNF- $\alpha$  [37]. Given that the RGC axons within the LC are unmyelinated, it is possible that these levels of strain could also be increasing the permeability of the axons themselves, hindering the propagation of action potentials and contributing to axon loss.

From a mechanical perspective, the high strains in the LC pores are partially explained by the fact that the lamina beams thin when stretched thereby increasing the area of the pores. Our sensitivity studies indicate that the peak strains in the neural tissue are influenced by the stiffness and non-linearity of the connective tissues, with a 2x increase in collagen stiffness resulting in a 38% reduction in mean 1<sup>st</sup> principal neural tissue strain. The degree of fiber anisotropy in the connective tissues had almost no effect on the distribution of strains in the neural tissues, this is similar to the findings of Zhang et al. who found that the anisotropy of the LC had little effect on the strains in the LC [13]. Although this may be true for the lamina, we note, that both the study by Zhang and other modeling studies have found that the degree of anisotropy in the sclera is influential on the strains in the LC [13, 15]. The stiffness of the neural tissue itself also had only a small influence on the neural tissue strains as a 10x increase in neural tissue stiffness reduced the mean 1<sup>st</sup> principal strain by only 11%. Further the mechanical properties generally had little effect on the patterns of pore-to-pore variability. These findings,

coupled with the fact that the direction of the 1<sup>st</sup> principal strain followed along the direction of the beams, suggests that the magnitude and patterns of insult are primarily due to the structure and organization of the laminar beams.

Another finding of this work is that the pores closest to the scleral boundary experienced the largest 1<sup>st</sup> principal strains and the most negative 2<sup>nd</sup> principal strains. This indicates not only that these pores undergo large deformations, but that the neural tissues within suffer high shear deformations. Most previous models predict this behavior, largely due to the compliance mismatch between the sclera and the LC, however, we see this in our microstructure models in which the material properties of the scleral collagen and laminar beams are identical. The prediction of high mechanical insult at the scleral boundary is particularly interesting given that glaucomatous axon loss initiates at the periphery of the lamina [7].

In our study using second harmonic generation, we found that an IOP elevation of 35 mmHg (10 to 45 mmHg or 15 to 50 mmHg) resulted in localized 1<sup>st</sup> principal strain exceeding 10 and even 20%. Furthermore, our data suggested that the amount of stretch or compression varied largely from one pore to another. Peak strains exceeding 10% have been reported by Midgett and colleagues who also used second harmonic generation to measure the deformation of human LCs [20]. While both of these studies were done *ex vivo*, we have also recently measured strains *in vivo* in the LC of rhesus macaque monkeys under various levels of IOP and intracranial pressure using optical coherence tomography [19]. In this study we again found IOP-induced local tensile and compressive strains in excess of 20%. The strains predicted using our microstructure models in this work are more in line with these experimental findings than those predicted by any previous models, indicating that it is essential to consider the connective tissue and neural tissue of the LC as distinct materials. In fact, we are currently studying the degree to which microstructural details are necessary for the accurate characterization of LC biomechanics.

A few other models have considered the properties of the neural tissue and the collagenous beams separately. Bellezza et al. modeled coarse versions of the lamina with a few collagen beams and rectangular LC pores and reported higher stresses in the collagenous beams than in the neural tissue [8]. Sander et al., created a multiscale analytical model to study stresses at the pore level and also found an amplification of stresses within the LC microstructure. Both these models, however, used simplified generic geometries with symmetric beams and pores and isotropic, linear elastic material properties. Our model is the first to use highly-detailed specimen-specific geometries, and non-linear material properties.

While the multiscale modeling approach we have used provides a reasonable framework for understanding important biomechanical phenomena, it is important to note its limitations. We chose to model the microstructure of the LC at a very high resolution, and therefore in this first work we only created microscale models of LC regions, not the whole LC. Our results suggest that the increased resolution provided novel insights that were not previously attainable. Further, our two-level approach provides reasonable boundary conditions for the multiscale models in-line with other studies [13]. The technique we have presented is compatible with high resolution models of the whole LC, being limited only by the computer memory available during simulation. We based our models on histology slides because they allow high resolution measurements of ONH microstructure and collagen fiber orientation, in the primary plane of the connective tissue microstructure [21, 22]. Other imaging techniques do not provide out-of-plane resolution comparable to the in-plane resolution we can get with polarized light microscopy. Further, we have also demonstrated that our tissue processing methodology, formalin fixation and cryosectioning, does not induce significant tissue deformation or shrinkage [21], which has been found in other studies [38]. This gives us confidence that the dimensions of the microstructure in our models are similar to the dimensions in situ. While our approach does not yet incorporate the curvature and out of plane orientation of the lamina beams and RGC axons, the out-of-plane stress in the lamina is thought to be small compared to the in-plane stress [13, 39] and our model allows us to study the response of the LC to this primary loading. Thus, we believe our approach is reasonable given our aims.

There is no published experimental data on the non-linear material properties of sheep lamina beams, sclera and optic nerve tissue. We chose to use material properties for the connective tissues which were based on the properties of human scleral tissue obtained via inflation testing. Given that human scleral stiffness has been well characterized [15, 27, 28, 40, 41], we deemed this to be a reasonable assumption. More challenging was the choice of neural tissue properties. There were three key considerations when we decided to use properties from a study on guinea pig white matter [26]. 1) The material properties in the study were determined using tensile testing rather than indentation. This was important as the primary mode of deformation in our study was tensile. 2) The material properties reported by the study were hyperelastic and anisotropic to account for both the large strains and reduced cross-axon direction stiffness as compared to the axon direction. This was essential as our models primarily examine the stretch in the cross-axon direction. 3) The experiments were done on nerve tissue with both the pia and gray matter excised. Although we would have preferred to use material properties from human or sheep, we reasoned that these considerations were just as important.

No matter what our choice of properties, they would still be approximation of the in-vivo specimen specific properties, and this is why we carried out a sensitivity analysis. We found that the connective tissue stiffness influenced the peak tensile and compressive strains, while the neural tissue stiffness had little effect. Connective tissue stiffness in the sclera is known to vary between individuals and with age and disease [27-29, 40]. Experimental determination of the mechanical properties of the LC beams themselves would improve future models and provide valuable insight into the mechanics of the LC.

While we have created a high resolution model that distinguishes the neural tissues from the collagenous beams of the lamina, our model still treats the neural tissue and collagenous beams as homogenous continuums. In reality, the neural tissues are composed of mixtures of RGC axons and glial cells which bind to each other and to the collagenous beams through transmembrane biochemical bonds such as cadherins and integrins [42]. These bonds may fail under high strains which may reduce the deformation of the axons and neural tissues. However, the disruption of cell-matrix bonding and cell-cell interactions would likely lead to changes in cell signaling and behavior and could induce remodeling, inflammation or even apoptosis. Hence, the high strains predicted by our model may best be understood as estimates of the risk for biomechanical insult. More experimental studies of cell-matrix biomechanics are needed before these types of interactions could be included in our models. Likewise, we have made assumptions about the collagen of the LC beams. In particular, we assume that the collagen beams are composed of a family of collagen fibers which undergo affine deformations. Although this approach and its assumptions are well accepted for mechanical models on the length scale of the posterior sclera [15, 43, 44], it is not necessarily the case that the deformation of the collagen in the LC beams is affine. In fact, studies have shown in other tissues that collagen fibrils and fibers may undergo non-affine deformations on the micron scale, particularly when loaded in the cross-fiber direction [45, 46]. Given the length scale of the LC beams, ~15-100 microns, and the fact that the collagen in the beams is aligned along the direction of loading, we suspect that the assumption of affine deformation is reasonable; however experimental studies using high resolution imaging would be needed to verify this.

## 5. Conclusion

When models consider the microstructure of the LC, the mechanical insult within the neural tissues of the optic nerve at the level of the LC exceeds the levels predicted by previous models, and is in agreement with recent experimental evidence. These levels of deformation



have been shown to be sufficient to activate the astrocytes residing in the neural tissue pores and may be detrimental to the RGC axons themselves.

**Acknowledgements:**

We would like to thank Emma Chen for assisting with image segmentation and Danielle Hu for assisting in the collection, stitching, and registering of images. This work was supported in part by National Institutes of Health grant R01-EY023966, R01-EY025011, P30-EY008098 and T32-EY017271 (Bethesda, MD) and the Eye and Ear Foundation (Pittsburgh, PA).

**References:**

- [1] Burgoyne CF. A biomechanical paradigm for axonal insult within the optic nerve head in aging and glaucoma. *Experimental eye research* 2011;93:120-32.
- [2] Hernandez MR. The optic nerve head in glaucoma: Role of astrocytes in tissue remodeling. *Progress in Retinal and Eye Research* 2000;19:297-321.
- [3] Sigal IA, Ethier CR. Biomechanics of the optic nerve head. *Experimental eye research* 2009; p. 799-807.
- [4] Quigley HA. Reappraisal of the mechanisms of glaucomatous optic nerve damage. *Eye* (London, England) 1987;1 ( Pt 2):318-22.
- [5] Bengtsson B, Heijl A. A long-term prospective study of risk factors for glaucomatous visual field loss in patients with ocular hypertension. *J Glaucoma* 2005;14:135-8.
- [6] Francis BA, Singh K, Lin SC, Hodapp E, Jampel HD, Samples JR, Smith SD. Novel Glaucoma Procedures: A Report by the American Academy of Ophthalmology. *Ophthalmology* 2011;118:1466-80.
- [7] Quigley HA, Addicks EM, Green WR, Maumenee AE. Optic nerve damage in human glaucoma. II. The site of injury and susceptibility to damage. *Arch Ophthalmol* 1981;99:635-49.
- [8] Bellezza AJ, Hart RT, Burgoyne CF. The optic nerve head as a biomechanical structure: Initial finite element modeling. *Investigative Ophthalmology and Visual Science* 2000;41:2991-3000.
- [9] Sigal IA, Flanagan JG, Tertinegg I, Ethier CR. Finite element modeling of optic nerve head biomechanics. *Investigative ophthalmology & visual science* 2004;45:4378-87.
- [10] Sigal IA, Flanagan JG, Tertinegg I, Ethier CR. Modeling individual-specific human optic nerve head biomechanics. Part I: IOP-induced deformations and influence of geometry. *Biomech Model Mechanobiol* 2009;8:85-98.
- [11] Sander EA, Downs JC, Hart RT, Burgoyne CF, Nauman EA. A cellular solid model of the lamina cribrosa: mechanical dependence on morphology. *Journal of biomechanical engineering* 2006;128:879-89.
- [12] Downs JC, Roberts MD, Burgoyne CF, Hart RT. Multiscale finite element modeling of the lamina cribrosa microarchitecture in the eye. *Conference proceedings : Annual International Conference of the IEEE Engineering in Medicine and Biology Society IEEE Engineering in Medicine and Biology Society Conference* 2009;2009:4277-80.
- [13] Zhang L, Albon J, Jones H, Gouget CLM, Ethier CR, Goh JCH, Girard MJA. Collagen Microstructural Factors Influencing Optic Nerve Head Biomechanics. *Investigative Ophthalmology & Visual Science* 2015;56:2031-42.
- [14] Campbell IC, Coudrillier B, Mensah J, Abel RL, Ethier CR. Automated segmentation of the lamina cribrosa using Frangi's filter: a novel approach for rapid identification of tissue

- volume fraction and beam orientation in a trabeculated structure in the eye. *J R Soc Interface* 2015;12:20141009.
- [15] Coudrillier B, Boote C, Quigley HA, Nguyen TD. Scleral anisotropy and its effects on the mechanical response of the optic nerve head. *Biomech Model Mechanobiol* 2013;12:941-63.
- [16] Sigal IA, Flanagan JG, Ethier CR. Factors influencing optic nerve head biomechanics. *Investigative ophthalmology & visual science* 2005;46:4189-99.
- [17] Ayyalasomayajula A, Park RI, Simon BR, Vande Geest JP. A porohyperelastic finite element model of the eye: the influence of stiffness and permeability on intraocular pressure and optic nerve head biomechanics. *Computer methods in biomechanics and biomedical engineering* 2016;19:591-602.
- [18] Sigal IA, Grimm JL, Jan NJ, Reid K, Minckler DS, Brown DJ. Eye-specific IOP-induced displacements and deformations of human lamina cribrosa. *Invest Ophthalmol Vis Sci* 2014;55:1-15.
- [19] Tran H, Grimm J, Wang B, Smith M, Gogola A, Nelson S, Tyler-Kabara E, Schuman J, Wollstein G, Sigal I. Mapping in-vivo optic nerve head strains caused by intraocular and intracranial pressures. *Proc of SPIE Vol2017*. p. 100670B-1.
- [20] Midgett DE, Pease ME, Jefferys JL, Patel M, Franck C, Quigley HA, Nguyen TD. The pressure-induced deformation response of the human lamina cribrosa: Analysis of regional variations. *Acta Biomaterialia* 2017.
- [21] Jan N-J, Grimm JL, Tran H, Lathrop KL, Wollstein G, Bilonick RA, Ishikawa H, Kagemann L, Schuman JS, Sigal IA. Polarization microscopy for characterizing fiber orientation of ocular tissues. *Biomed Opt Express* 2015;6:4705-18.
- [22] Jan NJ, Lathrop K, Sigal IA. Collagen Architecture of the Posterior Pole: High-Resolution Wide Field of View Visualization and Analysis Using Polarized Light Microscopy. *Invest Ophthalmol Vis Sci* 2017;58:735-44.
- [23] Schindelin J, Arganda-Carreras I, Frise E, Kaynig V, Longair M, Pietzsch T, Preibisch S, Rueden C, Saalfeld S, Schmid B, Tinevez JY, White DJ, Hartenstein V, Eliceiri K, Tomancak P, Cardona A. Fiji: an open-source platform for biological-image analysis. *Nature methods* 2012;9:676-82.
- [24] Preibisch S, Saalfeld S, Tomancak P. Globally optimal stitching of tiled 3D microscopic image acquisitions. *Bioinformatics* 2009;25:1463-5.
- [25] Zhang TY, Suen CY. A Fast Parallel Algorithm for Thinning Digital Patterns. *Commun Acm* 1984;27:236-9.
- [26] Galle B, Ouyang H, Shi R, Nauman E. A transversely isotropic constitutive model of excised guinea pig spinal cord white matter. *Journal of Biomechanics* 2010;43:2839-43.
- [27] Coudrillier B, Pijanka JK, Jefferys J, Sorensen T, Quigley HA, Boote C, Nguyen TD. Effects of Age and Diabetes on Scleral Stiffness. *Journal of biomechanical engineering* 2015.

- [28] Fazio MA, Grytz R, Morris JS, Bruno L, Girkin CA, Downs JC. Human Scleral Structural Stiffness Increases More Rapidly With Age in Donors of African Descent Compared to Donors of European Descent Scleral Stiffness Changes With Age and Race. *Investigative Ophthalmology & Visual Science* 2014;55:7189-98.
- [29] Albon J, Purslow PP, Karwatowski WS, Easty DL. Age related compliance of the lamina cribrosa in human eyes. *Br J Ophthalmol* 2000;84:318-23.
- [30] Chai DN, P.; Jester, B.E.; Reid, K.M.; Juhasz T.; Jester, J.V.; Minckler, D.S.; Brown, D.J. Indentation Testing of the Optic Nerve Head and Posterior Sclera. 2014 2014;3:18-27.
- [31] Maas SA, Ellis BJ, Ateshian GA, Weiss JA. FEBio: finite elements for biomechanics. *J Biomech Eng* 2012;134:011005.
- [32] Moerman KM. GIBBON (Hylobates Lar). Zenodo2016.
- [33] Krizaj D, Ryskamp DA, Tian N, Tezel G, Mitchell CH, Slepak VZ, Shestopalov VI. From mechanosensitivity to inflammatory responses: new players in the pathology of glaucoma. *Curr Eye Res* 2014;39:105-19.
- [34] Islas L, Pasantes-Morales H, Sanchez JA. Characterization of stretch-activated ion channels in cultured astrocytes. *Glia* 1993;8:87-96.
- [35] Exler RE, Guo X, Chan D, Livne-Bar I, Vivic N, Flanagan JG, Sivak JM. Biomechanical insult switches PEA-15 activity to uncouple its anti-apoptotic function and promote erk mediated tissue remodeling. *Experimental Cell Research* 2016;340:283-94.
- [36] Rogers RS, Dharsee M, Ackloo S, Sivak JM, Flanagan JG. Proteomics Analyses of Human Optic Nerve Head Astrocytes Following Biomechanical Strain. *Molecular & Cellular Proteomics* 2012;11:M1111.012302-M1111.
- [37] Salvador E, Burek M, Förster CY. Stretch and/or oxygen glucose deprivation (OGD) in an in vitro traumatic brain injury (TBI) model induces calcium alteration and inflammatory cascade. *Frontiers in Cellular Neuroscience* 2015;9:323.
- [38] Roberts MD, Liang Y, Sigal Ia, Grimm J, Reynaud J, Bellezza A, Burgoyne CF, Downs JC. Correlation between local stress and strain and lamina cribrosa connective tissue volume fraction in normal monkey eyes. *Investigative Ophthalmology and Visual Science* 2010;51:295-307.
- [39] Downs JC, Roberts MD, Burgoyne CF. The Mechanical Environment of the Optic Nerve Head in Glaucoma. *Optometry and vision science : official publication of the American Academy of Optometry* 2008;85:425-35.
- [40] Grytz R, Fazio MA, Libertiaux V, Bruno L, Gardiner S, Girkin CA, Downs JC. Age- and race-related differences in human scleral material properties. *Invest Ophthalmol Vis Sci* 2014;55:8163-72.
- [41] Coudrillier B, Pijanka JK, Jefferys JL, Goel A, Quigley HA, Boote C, Nguyen TD. Glaucoma-related Changes in the Mechanical Properties and Collagen Micro-architecture of the Human Sclera. *PLoS One* 2015;10:e0131396.

- [42] Elkington AR, Inman CB, Steart PV, Weller RO. The structure of the lamina cribrosa of the human eye: an immunocytochemical and electron microscopical study. *Eye (London, England)* 1990;4 ( Pt 1):42-57.
- [43] Girard MJA, Downs JC, Burgoyne CF, Suh J-KF. Peripapillary and posterior scleral mechanics--part I: development of an anisotropic hyperelastic constitutive model. *Journal of biomechanical engineering* 2009;131:051011.
- [44] Grytz R, Sigal IA, Ruberti JW, Meschke G, Downs JC. Lamina Cribrosa Thickening in Early Glaucoma Predicted by a Microstructure Motivated Growth and Remodeling Approach. *Mechanics of materials : an international journal* 2012;44:99-109.
- [45] Lake SP, Cortes DH, Kadlowec JA, Soslowsky LJ, Elliott DM. Evaluation of affine fiber kinematics in human supraspinatus tendon using quantitative projection plot analysis. *Biomech Model Mechanobiol* 2012;11:197-205.
- [46] Hepworth DG, Steven-fountain A, Bruce DM, Vincent JFV. Affine versus non-affine deformation in soft biological tissues, measured by the reorientation and stretching of collagen fibres through the thickness of compressed porcine skin. *Journal of Biomechanics* 2001;34:341-6.

## TABLES:

**Table 1. Baseline material properties**

Parameter	Collagenous Tissue	Neural Tissue
$\xi$ - Fiber Stiffness (kPa)	1600	69.4
$\alpha$ – Fiber Non-linearity	120	1
$C_1$ – 1 <sup>st</sup> Mooney-Rivlin Constant (kPa)	150	0.876
$C_2$ – 2 <sup>nd</sup> Mooney-Rivlin Constant (kPa)	0	0.614
$\kappa$ - Fiber Dispersion	2	Perfectly Aligned
K - Bulk Modulus (kPa)	5000	0.412

**Table 2. Collagenous tissue properties for sensitivity study**

Parameter	Stiff	Compliant	Linear	Non-Linear
$\xi$ - Fiber Stiffness (kPa)	3200	800	1860	1370
$\alpha$ – Fiber Non-linearity	120	120	0	240
$C_1$ – 1 <sup>st</sup> Mooney-Rivlin Constant (kPa)	300	75	150	150
$C_2$ – 2 <sup>nd</sup> Mooney-Rivlin Constant (kPa)	0	0	0	0
K - Bulk Modulus (kPa)	5000	5000	5000	5000

**Figure Captions:**

**Figure 1. The anatomy of the eye and optic nerve head.** (Top) A longitudinal section of the eye is shown. Retinal ganglion cell axons (shown in red) exit the eye through a collagenous structure called the lamina cribrosa (highlighted in green) as they form the optic nerve. (Bottom) A coronal section of the optic nerve head showing the collagenous microstructure.

**Figure 2. Multiscale polarized light histology.** Sheep optic nerve heads (ONH) were serially sectioned and imaged at low magnification. Polarized light microscopy was used to determine the collagen fiber energy, a measure of collagen density, and fiber orientation [21]. Colors in the images represent the fiber orientation. Sections were registered to one another to form a stack. These stacked images were used as the basis for the mesoscale models used for boundary conditions. Individual sections were then reimaged at higher magnification, and registered to the low magnification stacks. Regions from the individual sections were then used to create the microscale models. Scale bars are 1 mm unless otherwise indicated.

**Figure 3. Multiscale modeling approach.** For mesoscale models (Left), material properties were based on fiber orientation and fiber density information from serial histology. Uniform boundary pressure was applied to simulate the hoop stress caused by IOP. Displacement predictions were obtained to use as boundary conditions for the microscale models. For microscale models (Right), regions of from histology sections were imaged at high resolution and segmented into LC beams and neural tissue. A 3D reconstruction of the beams was used as the basis for the finite element mesh. Fiber orientation was taken directly from polarized light microscopy images.

**Figure 4. Microscale regions of interest.** Four regions of central lamina and three regions of peripheral lamina with sclera were modeled. The multicolored images in the left columns, are the energy data from polarized light microscopy colored by the mean fiber angle. The right hand columns show the segmented masks used to create the models. Regions are sorted by increasing connective tissue volume fraction (CTVF) in the modeled region. Eyes are lettered A-G and will be referred to by these letters throughout this report.

**Figure 5. 1<sup>st</sup> and 2<sup>nd</sup> principal strains for all models.** 1<sup>st</sup> principal strains were generally smaller in the central lamina models (A-D) as compared to the peripheral models (E-G). The magnitude of both strains varied from one pore to another. Strains peak in regions of the pores

near branch points in the collagen beams. 2<sup>nd</sup> principal strains were positive and fairly uniform in the central region models, however, the 2<sup>nd</sup> principal strain was more varied and sometimes negative near the sclera indicating high shear strains at these locations. Elements located within 10% of the total region length or width from an edge are not shown so as to prevent the interpretation of edge effects.

**Figure 6. The distribution of strains in the neural tissues.** (Left) Distribution of 1<sup>st</sup> principal strains. (Right) Distribution of 2<sup>nd</sup> Principal strains. Whiskers show the 5<sup>th</sup> and 95<sup>th</sup> percentile stretches. Boxes span the 25<sup>th</sup>-75<sup>th</sup> percentiles. Red lines represent the median. Peak and median 1<sup>st</sup> principal strains were highest in the peripheral regions. In the peripheral models, the median 2<sup>nd</sup> principal strain was lower than that in the central regions and the 5<sup>th</sup> percentile smallest stretch was negative.

**Figure 7. The direction of 1<sup>st</sup> principal strain for region G.** (Top) The collagen beams stretched primarily along the length of the beam, in the direction of fiber orientation. Since the 2<sup>nd</sup> principal strain in the beams was negative, this indicates that the beams thinned as the LC is stretched by IOP. (Bottom) The neural tissues stretched in various directions. An alternating pattern of 1<sup>st</sup> principal strain direction was seen in the three pores marked by red arrows. There was a tendency for the neural tissues to stretch perpendicular to the beam-pore interface, especially in narrow pores.

**Figure 8. 1<sup>st</sup> Principal stress in the LC beams.** Stress was highly concentrated in some areas of the beams. Stresses were largest near the midpoints of the beams and away from beam intersections. Stresses were higher in the peripheral regions near the sclera.

**Figure 9. Effect of neural tissue stiffness on neural tissue strain.** Increasing neural tissue stiffness 10-fold, generally reduced the 1<sup>st</sup> principal strain, however some pores had regions with increased neural tissue strains. The 2<sup>nd</sup> principal strain was primarily increased when the stiffness of the neural tissue was increased. The main effect of increasing neural tissue stiffness appeared to be a narrowing of the distribution of 1<sup>st</sup> and 2<sup>nd</sup> principal strains.

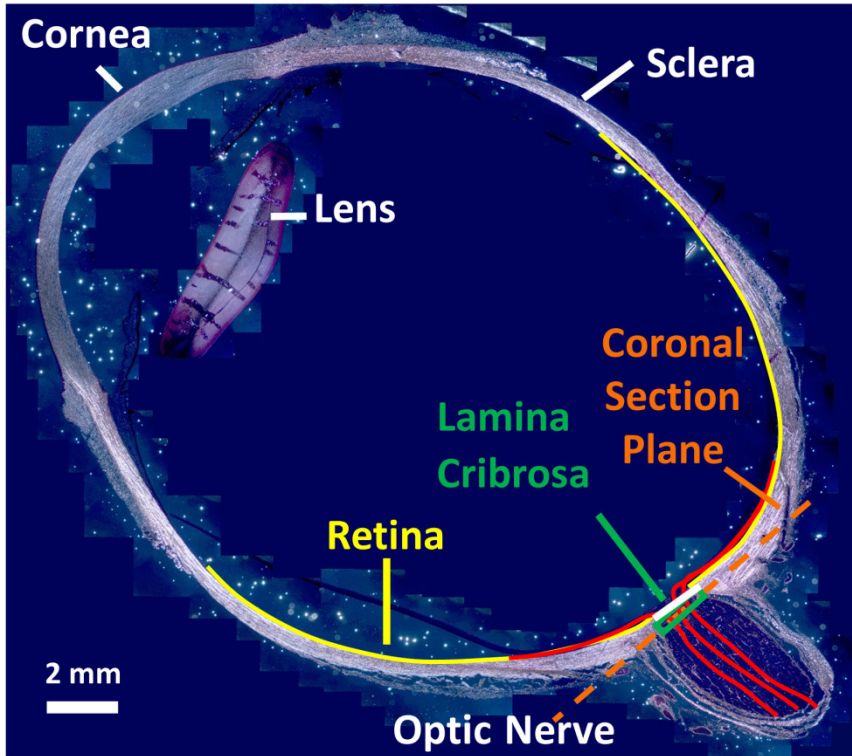
**Figure 10. The effects of connective tissue material properties on neural tissue strain.** (A) Material properties used in parametric variation study. Stiff and compliant cases represent a doubling or halving of the stiffness. In the linear case, the stiffness does not increase with increasing strain, and the stress at 2% equibiaxial strain is the same as with baseline material properties. In the non-linear case, the stiffness increases with strain at twice the rate as the baseline case, but again has the same stress as baseline at 2% equibiaxial strain. (B)



Distribution of 1<sup>st</sup> principal (left) and 2<sup>nd</sup> principal strain (right) for region G. Whiskers show the 5<sup>th</sup> and 95<sup>th</sup> percentile strains. Boxes span the 25<sup>th</sup>-75<sup>th</sup> percentiles. Red lines represent the median. Increased stiffness reduced the 1<sup>st</sup> principal strain and narrowed the distribution of both 1<sup>st</sup> and 2<sup>nd</sup> principal strains, indicating less deformation. Compliant collagen material properties had the opposite effect. Linear material properties resulted in a slightly wider distribution of 1<sup>st</sup> and 2<sup>nd</sup> principal strains, however the median strain was similar to baseline. Increased non-linearity did not result in major differences as compared to baseline.

**Figure 11. The effect of collagen fiber dispersion on neural tissue strain.** Distribution of 1<sup>st</sup> principal (Left) and 2<sup>nd</sup> principal strains (Right) for region G. Whiskers show the 5<sup>th</sup> and 95<sup>th</sup> percentile strains. Boxes span the 25<sup>th</sup>-75<sup>th</sup> percentiles. Red lines represent the median. An isotropic alignment of fibers and a wide distribution of fibers did not result in major changes in the distribution of neural tissue strains. A perfectly aligned distribution of fibers resulted in increased 1<sup>st</sup> principal strains and more negative 2<sup>nd</sup> principal strains indicating increased shear strains in the neural tissues.

Fig. 1 **Longitudinal Section**



**Coronal Section**

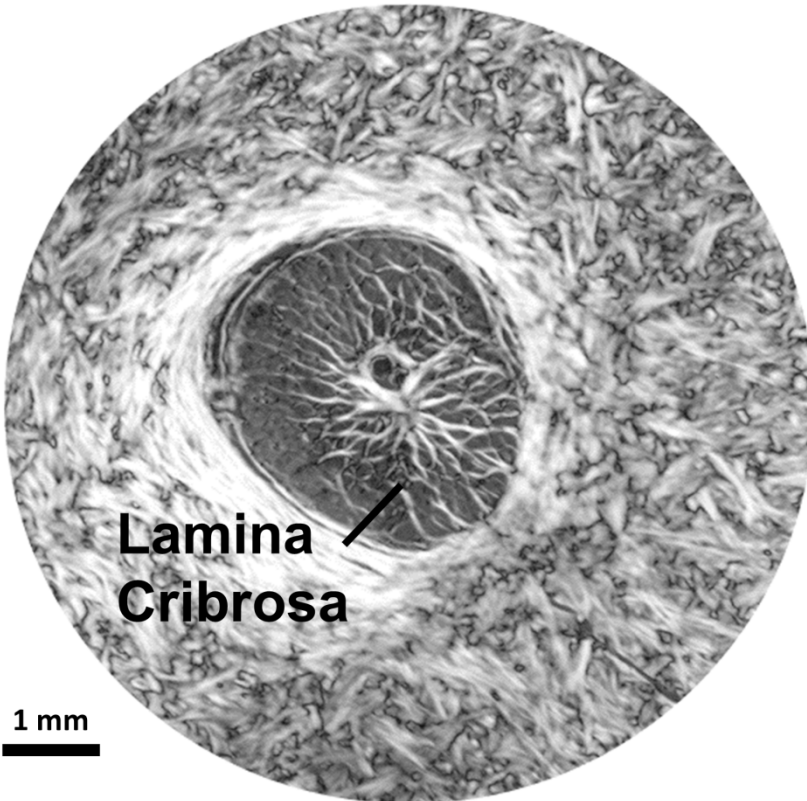
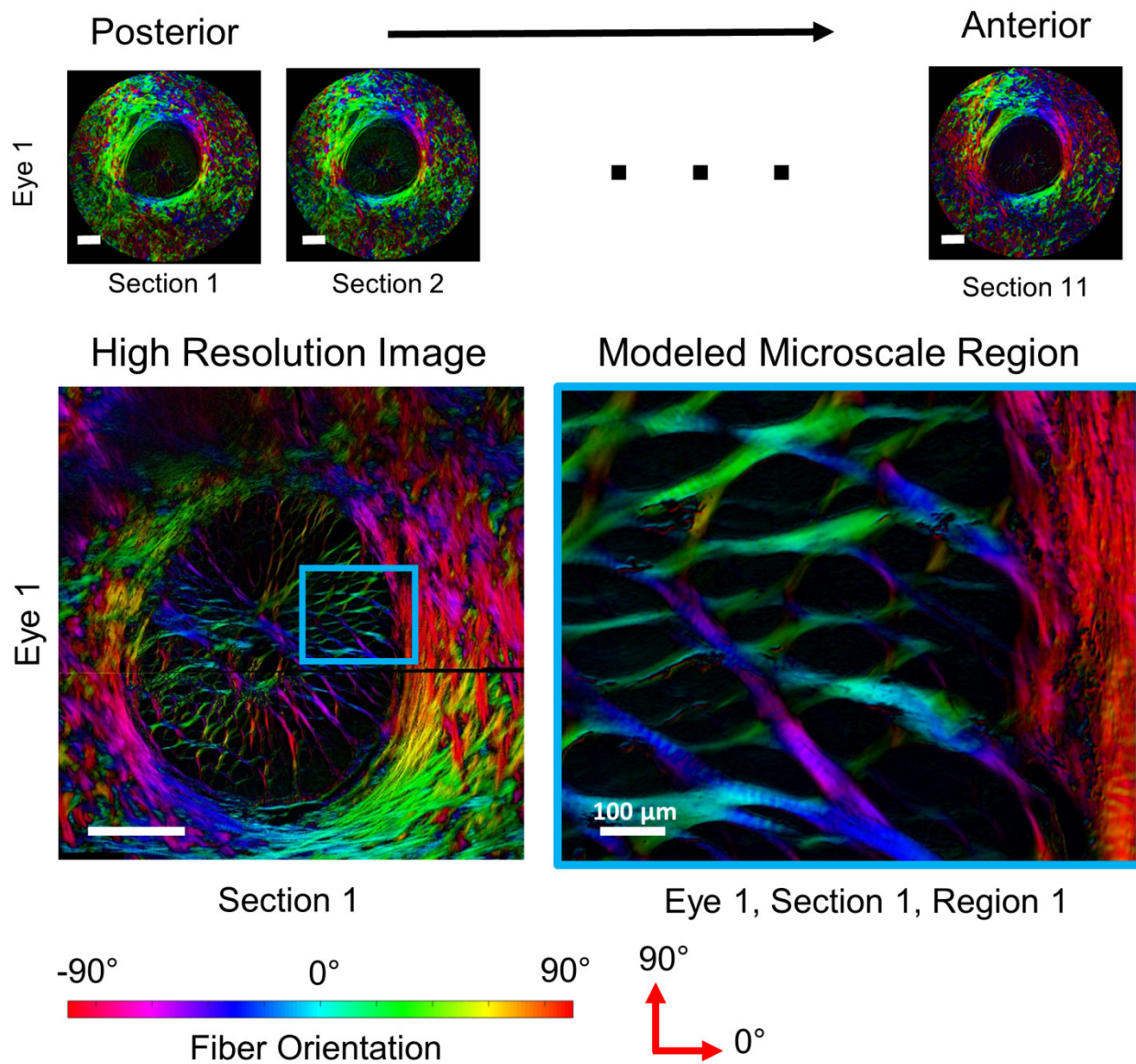


Fig. 2

## Coarse Resolution Serial Sections for Mesoscale Models



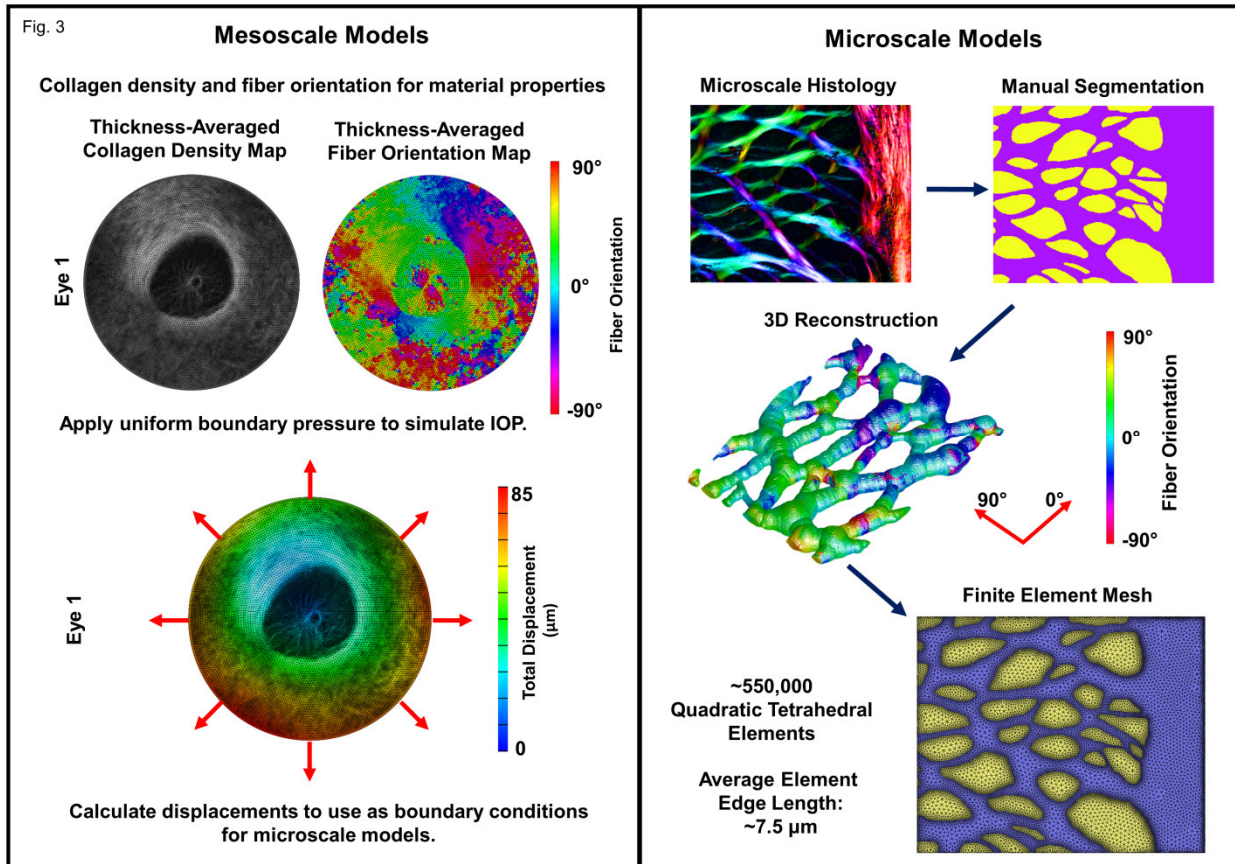


Fig. 4

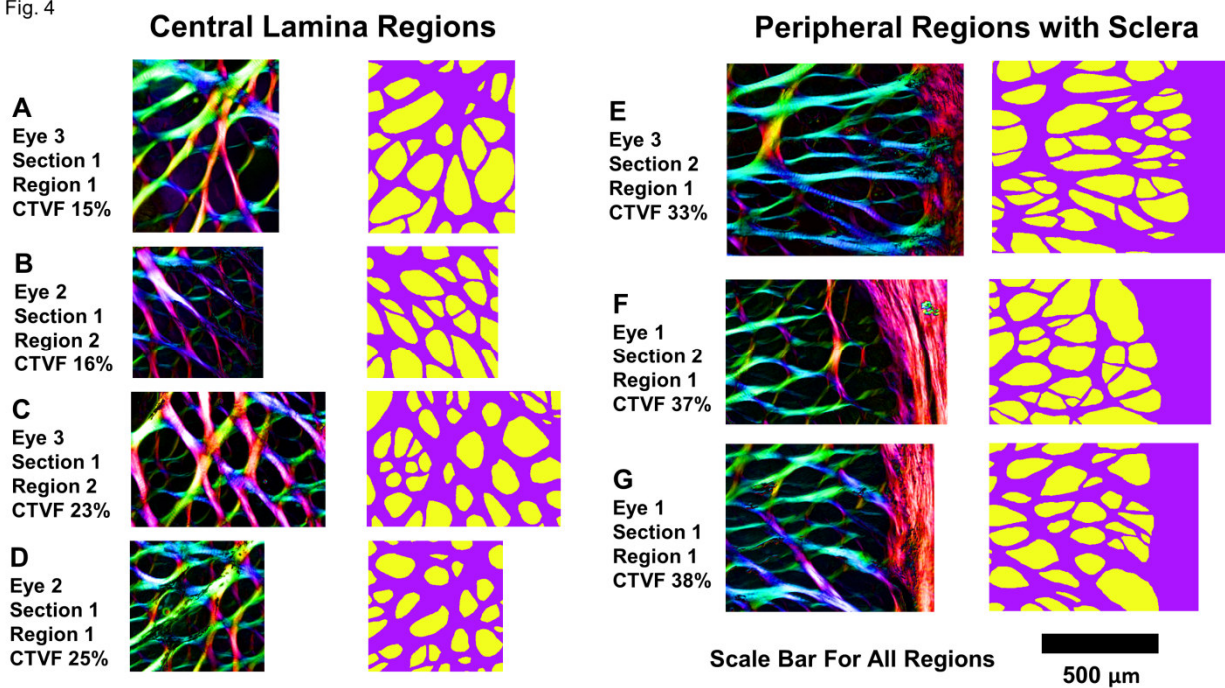


Fig. 5

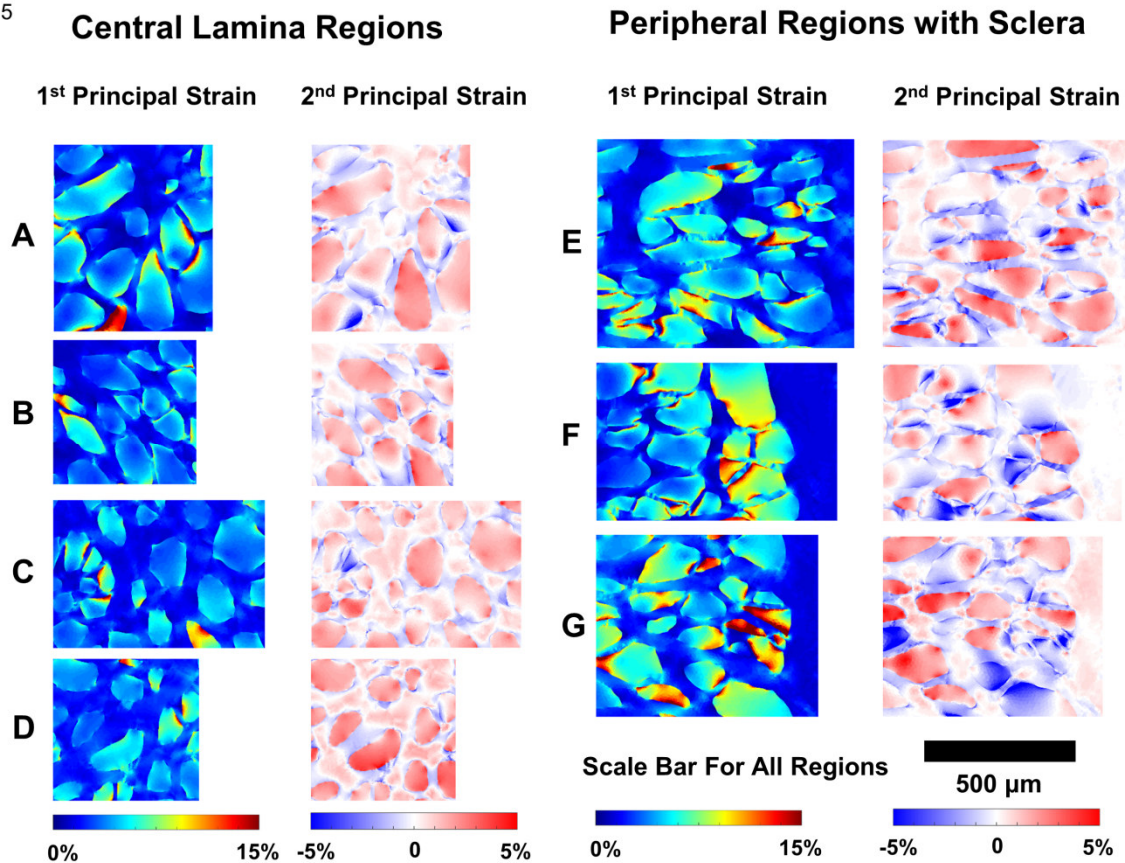


Fig. 6

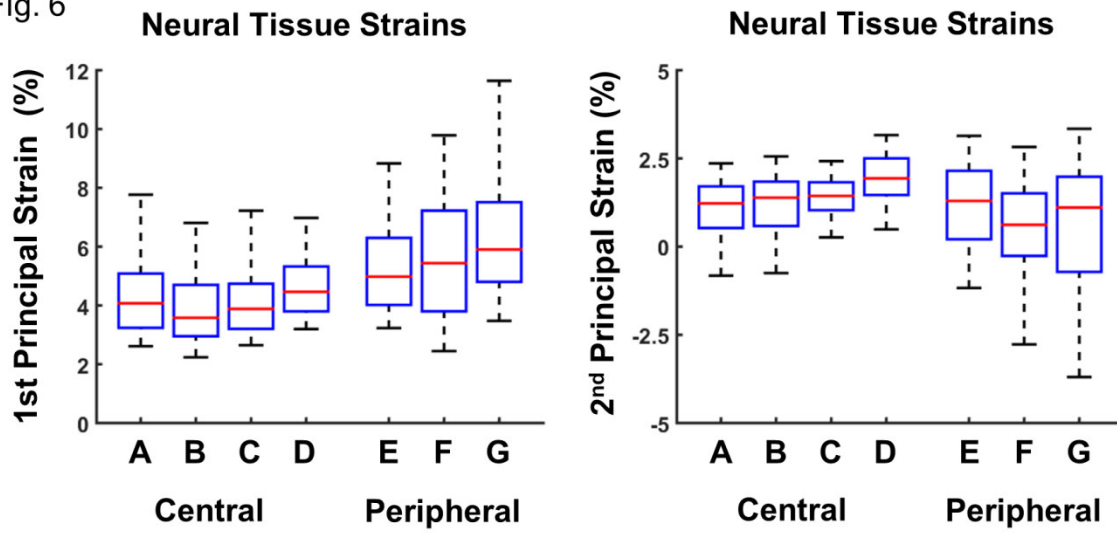
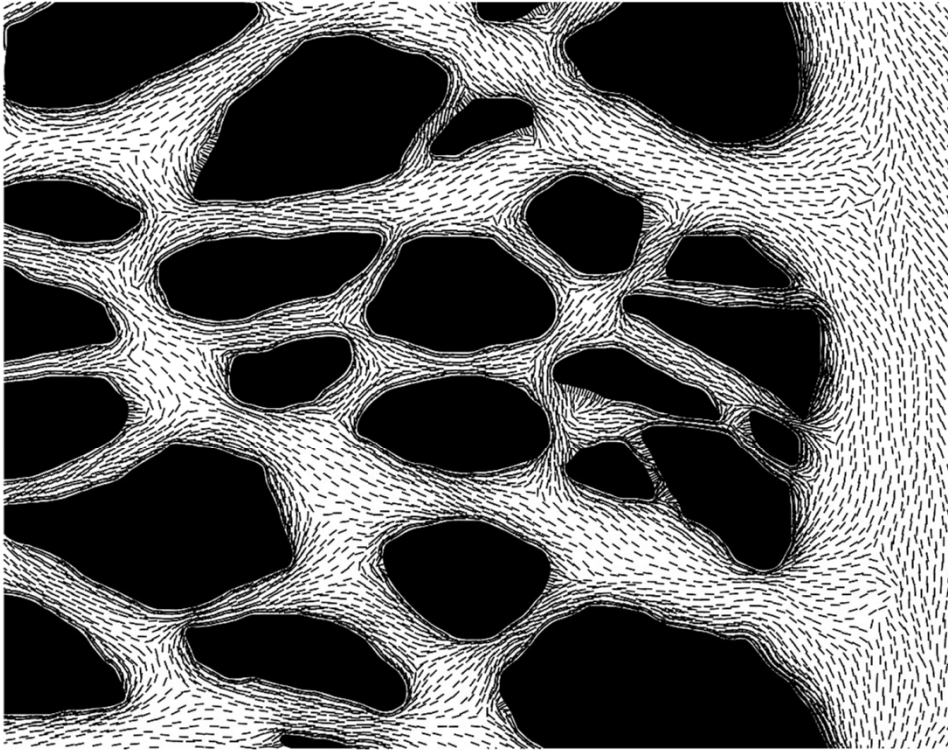


Fig. 7

Direction of 1<sup>st</sup> Principal Strain

Collagen Beams



Neural Tissue

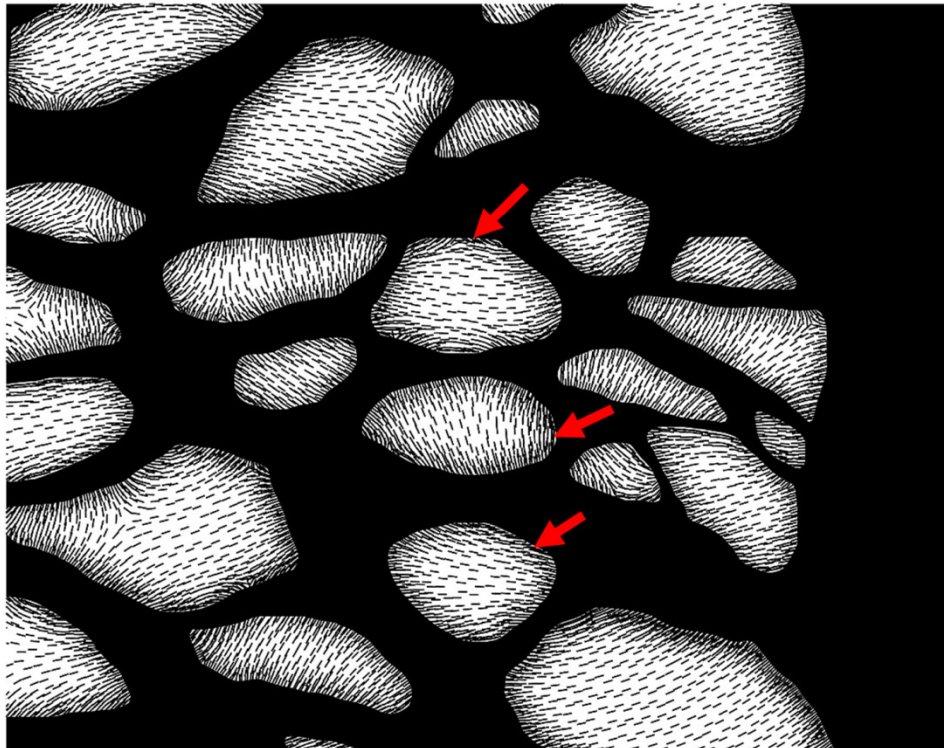




Fig. 8

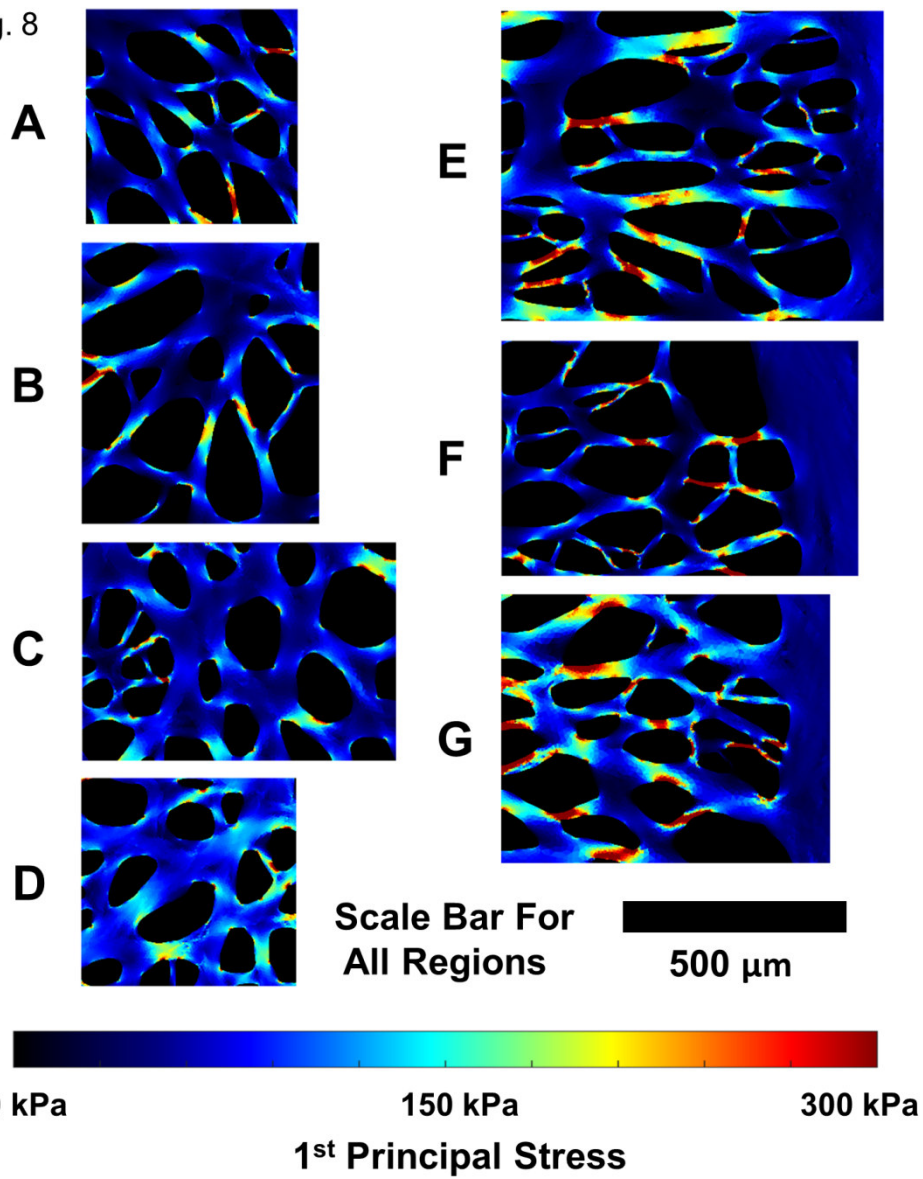
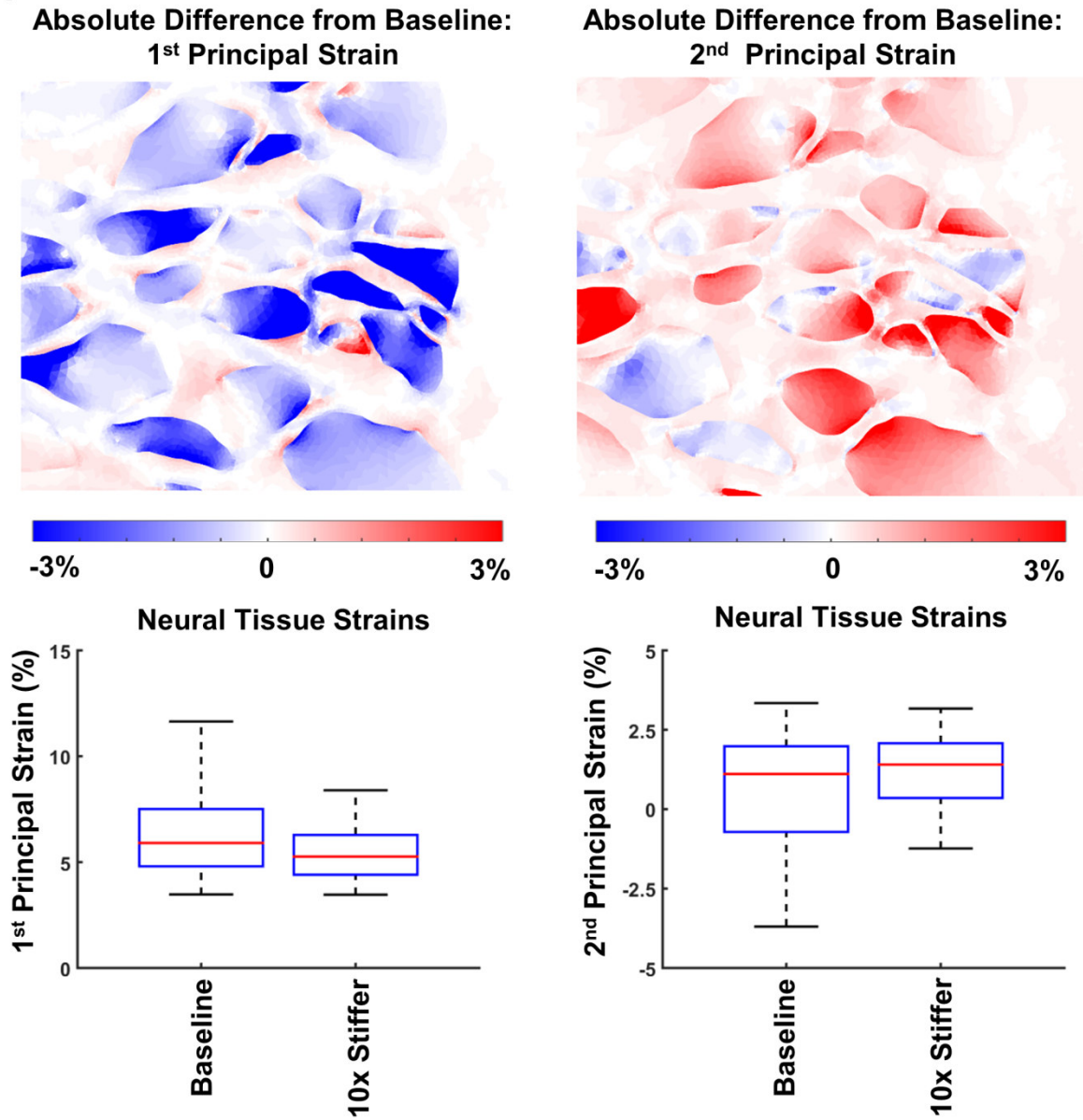


Fig. 9



ACC

Fig. 10

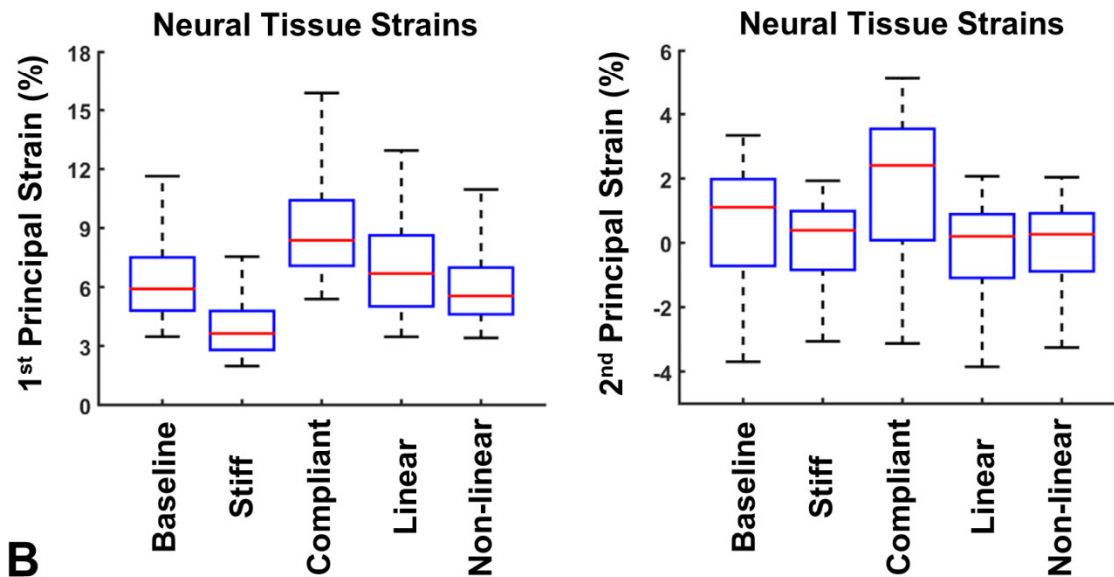
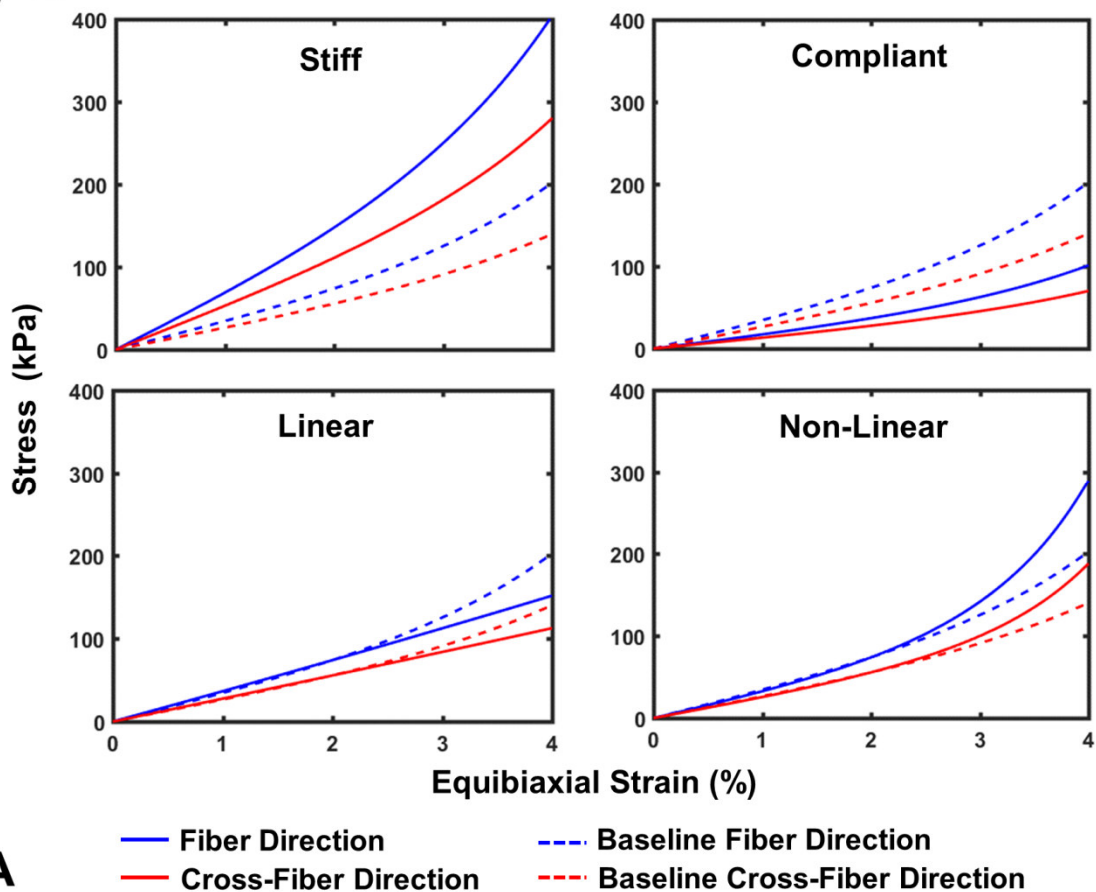
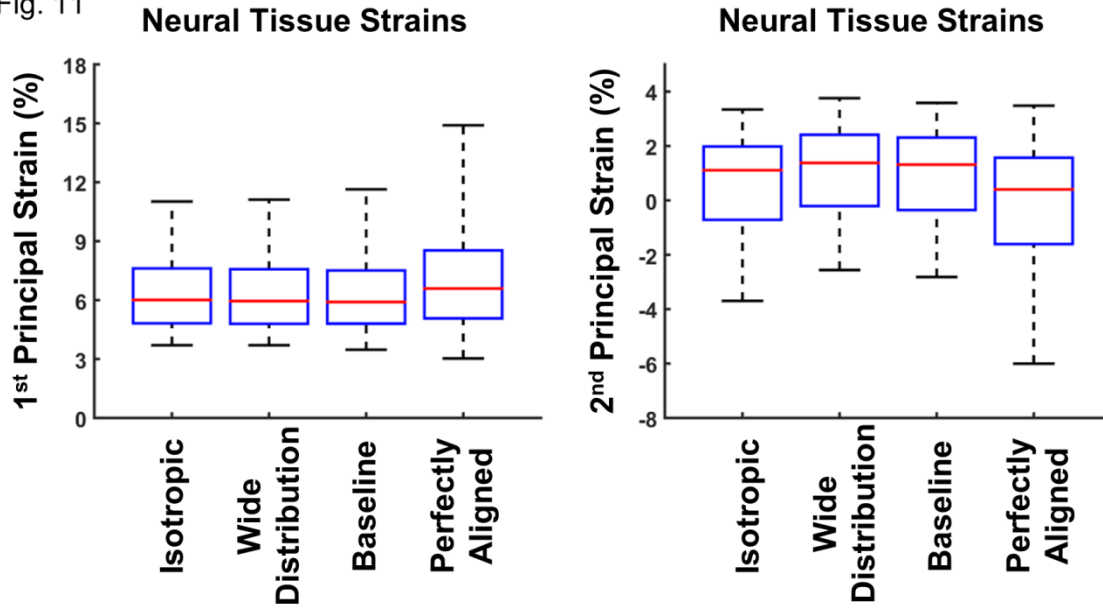


Fig. 11



**Statement of Significance**

The loss of visual function associated with glaucoma has been attributed to sustained mechanical insult to the neural tissues of the lamina cribrosa due to elevated intraocular pressure. Our study is the first computational model built from specimen-specific tissue microstructure to consider the mechanics of the neural tissues of the lamina separately from the connective tissue. We found that the deformation of the neural tissue was much larger than that predicted by any recent microstructure-aware models of the lamina. These results are consistent with recent experimental data and the highest deformations were found in the region of the lamina where glaucomatous damage first occurs. This study provides new insight into the complex biomechanical environment within the lamina.

